Climate Change and urban pressures intensify flood risk on the Gulf of Guinea coast

Authors

Joyce Kimutai, *Centre for Environmental Policy, Imperial College, London, UK*
Theodore Keeping, *Centre for Environmental Policy, Imperial College, London, UK*
Guigma Kiswedsida, *Red Cross Red Crescent Climate Centre, The Hague, The Netherlands (based in Ouagadougou, Burkina Faso)*
Rahinatu Sidiki Alare, Department of Geography, King's College London, London, UK
Etienne Kouakou, Chargé de Recherche à l'UNA, Chercheur Associé au CSRS
Lucia Mumo, Institute of Climate Change and Adaptation, University of Nairobi
Patricia Nying'uro *Kenya Meteorological Department*
Masambaya Fredrick, Institute of Climate Change and Adaptation, University of Nairobi
Izidine Pinto, *Royal Netherlands Meteorological Institute (KNMI), De Bilt, The Netherlands*
Roop Singh, *Red Cross Red Crescent Climate Centre, The Hague, The Netherlands (based in New Jersey, USA)*
Maja Vahlberg, *Red Cross Red Crescent Climate Centre, The Hague, the Netherlands; Swedish Red Cross, Stockholm, Sweden (based in Ubmeje/Umeå, Sweden)*
Senha Ganguly, *Red Cross Red Crescent Climate Centre, The Hague, The Netherlands)*
Vedanshee Pundeer, *Red Cross Red Crescent Climate Centre, The Hague, The Netherlands (based in New Delhi, India)*
Gerbrand Koren, *Copernicus Institute of Sustainable Development, Utrecht University, Utrecht, the Netherlands*
Friederike Otto, *Centre for Environmental Policy, Imperial College, London, UK*

Review authors

Sjoukje Philip, *Royal Netherlands Meteorological Institute (KNMI), De Bilt, The Netherlands*
Ben Clarke, *Centre for Environmental Policy, Imperial College, London, UK*
Julie Arrighi, *Red Cross Red Crescent Climate Centre, The Hague, The Netherlands; Global Disaster Preparedness Centre, American Red Cross, Washington D.C., USA; Tufts University, Massachusetts, USA (based in New York, USA)*

Cite as Kimutai, J. et al. (2026): Climate Change and urban pressures intensify flood risk on the Gulf of Guinea coast (WWA scientific report No. 86) World Weather Attribution. DOI:10.25560/131268

Main findings

- The floods affected a very densely populated region where rapid urbanisation and the expansion of formal and informal settlements into floodplains and conversion of natural vegetation to croplands have reduced natural drainage capacity and increased exposure to flooding. Population growth is projected to continue its upward trajectory in this region, further increasing exposure in the decades to come.
- The flood impacts extend far beyond the areas directly inundated. Disruptions to infrastructure, livelihoods, and agriculture can worsen food insecurity, and contaminated water and damaged sanitation and hygiene systems increase the risk of water-borne diseases in the coming week and months, particularly for children and people with pre-existing health conditions. This year's flooding is part of a pattern of similar floods that periodically occur in this region, eroding people's assets and ability to recover.
- The event is not rare in today's climate, which is 1.4°C warmer than it would have been at the beginning of the industrial period. A 3-day rainfall event of this magnitude is now expected to occur about once every 2-4 years in the study region.
- To assess if human-induced climate change influenced the heavy rainfall in the study region, we first determine if there is a trend in the observations. Results showed that observed 3-day rainfall has increased in intensity by about 23% over the study region since records began. Equivalently, an event like this is about five times more likely to occur today than it would have in a 1.4°C cooler climate. However uncertainties around these numbers are high and depend on which datasets are used.
- To quantify the role of human-induced climate change we also analyse climate models over the relatively small study region. Overall, the available climate models indicate only a very small increase in the likelihood of an event such as the one under study with about 4% increase in intensity. While the majority of the models show a trend toward more extreme precipitation events, they systematically underestimate the observed increase..sWhile most models show an increase in 3-day rainfall, supporting the conclusion that the observed increase is attributable, confidence in the estimated magnitude of the attributed change is constrained by the models' limited performance and by the fact that none were developed or calibrated specifically for the African continent. Consequently, combining model- and observation-based estimates to derive a single quantitative attribution result is not meaningful.
- Under a future warming scenario where the global temperature is 2.8°C higher than pre-industrial levels, climate models suggest that even wetter 3-day periods should be expected. Given that these events are not rare today, this means they will be common occurrences, and the region needs to prepare for much heavier events than those observed in 2026.
- Research has shown that sea level rise along the Gulf of Guinea coast has exceeded the global average, compounding the impacts of increasingly intense rainfall. Together, these changes are thus driving greater flood risk along the Gulf of Guinea than would result from rainfall intensification alone, increasing risks to densely populated cities and critical infrastructure.
- Floods and associated impacts will continue to occur unless significant efforts are made to reduce vulnerability and exposure to the floods. While the dominant form of flood adaptation in the region is physical infrastructure, a range of solutions is needed to address the impacts to

infrastructure, health, economic losses, and displacement that results from these floods. These can include increasing access to safe and affordable housing, improving drainage and sanitation systems, enforcing policies on safer construction, improving early warning dissemination, and greater participation of affected communities in planning.

1 Introduction

In West Africa, April-May marks the onset of the rainy season in coastal countries, often leading to heavy flooding (Anticipation Hub, 2025). Since June 2026, the coastal regions of the Gulf of Guinea countries, particularly Côte D'Ivoire, Ghana, Togo, Benin, and Nigeria, have witnessed exceptionally widespread extreme precipitation that led to the subsequent flood events. Ghana recorded one of its highest daily June monthly rainfall amounts since 1995 (OCHA, 2026, Ghana Business News, 2026). Weather reports show that on 29 June alone, 172 mm of rain was recorded in Abidjan, Côte d'Ivoire (OGIMET 2026) and more than 140 mm in Accra, Ghana (Egbejule, 2026). In Abidjan, more than 16% of extreme daily rainfall was recorded in June, with the government (on July 01, 2026) indicating that 59 deaths had been reported since the beginning of the rainy season (The Guardian 2026). Rainfall in West Africa is modulated by the seasonal migration of the Intertropical Convergence Zone (ITCZ) and, as such, experiences two distinct rainfall regimes depending on the latitude: bimodal along the coast and unimodal further inland over the Sahel (Tore et al 2022, Dunning et al 2016). The ITCZ is a key component of the West African Monsoon System, which peaks between June and August (Raj et al 2019). This monsoon system is triggered by the rapid northward shift of the ITCZ in late June, which is associated with an influx of moisture from the Gulf of Guinea and signals the rainfall season over these parts of the Sahel (Sultan & Janicot, 2000). Extreme rainfall during the monsoon is primarily generated by the mesoscale convective systems (MCSs), which frequently develop in association with African Easterly Waves (AEWs) under conditions of strong low-level moisture transport, enhanced moisture convergence, and favourable large-scale atmospheric circulation (Engel et al., 2017).

Recent evidence from the extreme rainfall event in Dakar, September 5, 2020, further demonstrates that cyclonic vortices associated with AEWs can enhance moisture transport and prolong convective activity, resulting in exceptionally high rainfall totals and widespread flooding (Diedhiou et al., 2024). These organised convective systems are responsible for many of the region's most damaging extreme rainfall-producing floods. Rainfall mechanisms are governed by the movement of two tropical air masses. The first flow is continental, hot, and dry, originating from the northeast. It comes from the Azores High located at 30° north. This is the northern trade wind, also called the harmattan because of the dust it carries from Sahelian countries. The second air flow is maritime, hot, humid, from the southwest. It comes from the Saint Helena High located at 30° south: this is the southern trade wind, also known as the monsoon, originating from the Atlantic Ocean. These two air masses meet in the Intertropical Convergence Zone (ITCZ). The ITCZ is characterized by seasonal north-south movements linked to the intensities of the Azores and Saint Helena Highs, which themselves follow the sun's zenith position in the tropics (Dhonneur, 1978; Hamatan et al., 2004; Kouassi, 2007; Dibi Kangah, 2010). The ITCZ reaches its southern (5° North) and northern (20-25° North) positions in December-January and July, respectively.

Heavy rainfall associated with mesoscale convective systems is a common occurrence during the April-October season (monsoon season) across the Gulf of Guinea region, although the intensity and the spatial extent of this event were exceptional (Rauch et al., 2025). Figure 1 shows the weather system evolution from 18-29 June 2026 over West Africa. The event was enhanced by strong southwesterly low level monsoon winds which transported large quantities of warm, moisture-rich air from the tropical Atlantic and Gulf of Guinea into the coastal belt. This enhanced low-level moisture region convergence and atmospheric instability, creating favourable conditions for the development of deep convection and organised mesoscale convective systems. These organised convective systems produced high-intensity rainfall across coastal areas, leading to widespread flooding.

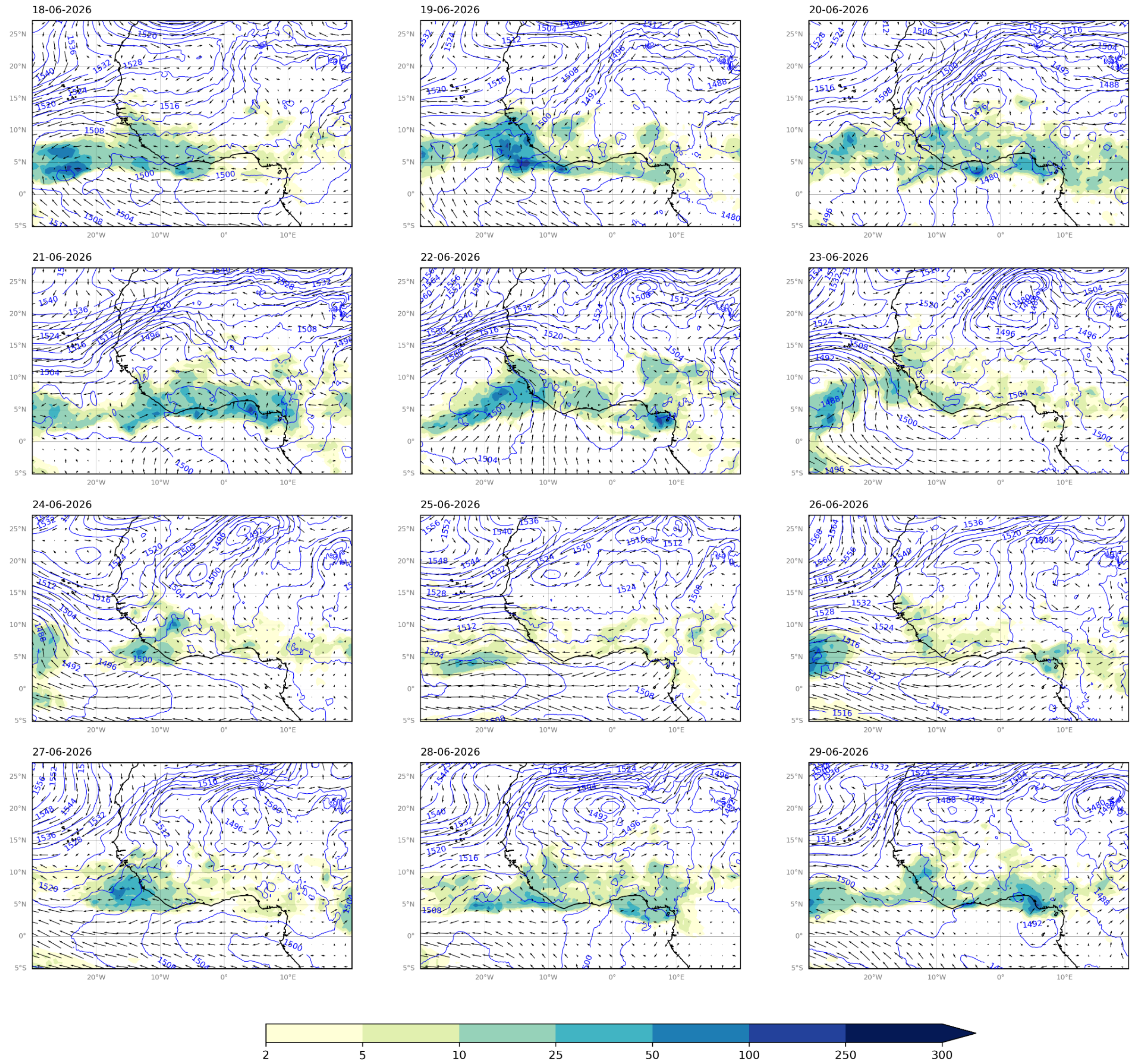

Figure 1. Daily rainfall (mm/day) overlaid with geopotential (m) height and winds (m/s) at 850 hPa. Data ERA5.

1.1 Impacts

The unexpected severity of the rainfall caused substantial infrastructure damage, disruption, and loss of life across Côte d'Ivoire, Ghana, Benin, Togo, and Nigeria (OCHA, 2026; Chanatry, 2026). More than 70 people were reported dead across the five countries, including at least 59 fatalities in Abidjan since mid-May (Wilson, 2026; Karikari, 2026 & OCHA, 2026). In several locations, the impacts were exacerbated by poor waste management and blocked drainage systems, which intensified urban runoff, inundated buildings, and displaced thousands of people (Agbo, 2026; Egbejule, 2026;

Karikari, 2026). The flooding also triggered cascading impacts on various economic sectors. In some areas, inundation damaged electrical infrastructure and caused fires, while in Nigeria, floodwater entered an international airport and temporarily suspended its operations (Oyedokun & Onyema, 2026; Egbejule, 2026). Economic activity, agricultural production, and livelihoods were significantly disrupted, resulting in widespread income losses (RFI, 2026). Flooded roads and the increased risk of crop disease under excessively wet conditions also raised concerns about reduced cocoa yields and higher prices, with potential implications for global supply (Prior, 2026). These impacts occurred against a backdrop of existing food insecurity, hence eroding household resilience. Area-level classifications for acute food insecurity in West Africa in May 2026 identified parts of Niger, Nigeria, and Cameroon as being under "stressed" or "crisis" conditions according to the Integrated Food Security Phase Classification scale (FEWS NET, 2026). Earlier FEWS NET analysis for August 2024 to January 2025 also showed that agricultural production shortfalls caused by agroclimatic shocks and trade constraints make seasonal flooding a persistent concern that can further exacerbate food insecurity across the region (FEWS NET, 2024). The ongoing floods have directly and indirectly impacted health systems by disrupting medical supply chains; physical injuries and death; food insecurity; and destruction of infrastructure, water, sanitation, and hygiene systems, which has heightened the vulnerability of the affected communities to vector- and water-borne diseases (OCHA,2026).

1.2 Rainfall extremes in West Africa Monsoon region

Floods are recurrent hazards across West Africa, particularly during the West African Monsoon season, when intense rainfall events can generate both pluvial and riverine flooding. Following severe Sahel droughts of the 1970s and 1980s, many parts of West Africa experienced reduced river flows and fewer large floods. However, since the 1990s, the region has experienced a partial recovery in rainfall accompanied by an increase in flood occurrence and severity in several catchments (Nka et al., 2015; Tazen et al., 2019). This increase has been accompanied by several catastrophic flood events, including the 2007 and 2009 floods, which affected hundreds of thousands of people and caused substantial loss of life and economic damage across the region. Between June and September 2009 alone, floods affected approximately 600,000 people and claimed at least 193 lives across 12 West African countries, with Burkina Faso, Senegal, Ghana, and Niger among the most severely affected (OCHA, 2008; Tschakert et al., 2010).

The increasing recurrence of floods across West Africa reflects the interaction of multiple drivers, including changes in rainfall characteristics,global teleconnection patterns amplification, and changes in mesoscale factors. Climate change is projected to increase temperatures and alter rainfall patterns across West Africa, leading to more frequent and intense extreme rainfall events (Diop et al., 2025; IPCC, 2022). Although uncertainties remain regarding future rainfall changes in West Africa because of model discrepancies in the simulation of the West African Monsoon (Diop et al., 2025), widespread increases in flood frequency and magnitude across West African catchments under future climate change are expected, particularly under the high-emission SSP5-8.5 scenario (Diop et al 2025; Ehret et al 2012).

In the Gulf of Guinea (GoG) region, rainfall events have become more intense (Bichet and Diedhiou 2018), increasing the likelihood of short-duration, high-intensity rainfall capable of triggering severe localised flooding. This changing rainfall regime has contributed to an increase in damaging flash floods in recent years, particularly in densely populated coastal cities. Climate change is also amplifying coastal flood risk through rising sea levels. Global mean sea level increased by approximately 11 cm between 1993 and 2023 (Hamlington et al., 2024), while sea level rise along the

Gulf of Guinea coast has exceeded the global average, with observed rates of approximately 3.9 mm yr^{-1} (Ghomsi et al., 2024). Rising sea levels are exacerbating coastal erosion, saltwater intrusion, and the frequency and severity of coastal flooding, thereby increasing risks to highly populated coastal settlements and critical infrastructure. Projections by Ghomsi et al. (2024) indicate that, under the SSP5-8.5 scenario, sea-level rise alone could substantially expand the extent of coastal inundation and displace up to two million people by the end of the century.

1.3 Event Definition

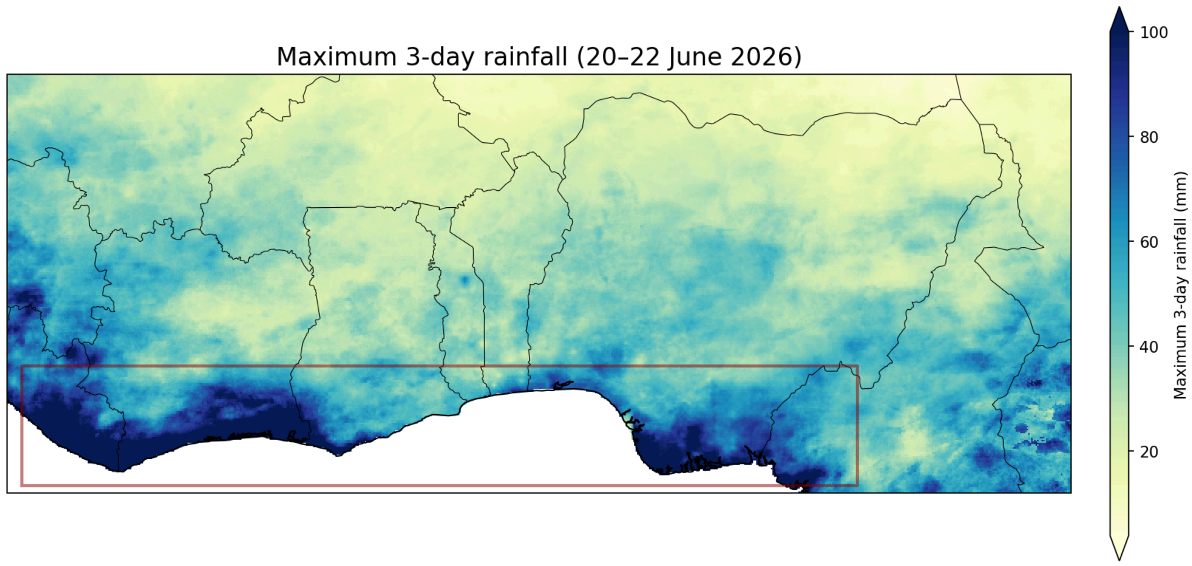

Figure 2 Map of the 3-day accumulated rainfall over the coast of west Africa during 20-22 June 2026. The study region (10W, 11E, 2N,7N) is outlined in red. Data: TAMSAT.

The flooding that affected the Gulf of Guinea countries between 15 and 30 June 2026 was associated with exceptionally heavy rainfall produced by organised mesoscale convective systems over the coastal belt of West Africa. These systems generated a series of intense rainfall bursts over several consecutive days, leading to widespread flooding across Côte d'Ivoire, Ghana, Togo, Benin, and Nigeria. While heavy rainfall associated with MCSs is a characteristic feature of the West African monsoon, the intensity and spatial extent of this event were exceptional. To capture the meteorological characteristics of the event, we define it as the maximum cumulative three-day (Rx3day; see Figure 3 -bottom) rainfall during June-July over the coastal monsoon region bounded by 10°W–11°E and 2°N–7°N (red box in Figure 2). For 2026, we use data till the time of writing of the report (July 10). A three-day accumulation was selected because the most severe flooding resulted from successive episodes of intense rainfall occurring over several days rather than from a single isolated rainfall event. This metric therefore better represents the rainfall accumulation responsible for the observed flooding and is less sensitive to small timing differences between in situ observations and gridded observations of daily rainfall (AX1).

The analysis focuses on the June–July period because it encompasses the first peak of the rainfall season over the Gulf of Guinea. As shown in Figure 3 (top), the climatological annual cycle exhibits a bimodal rainfall regime, with a primary maximum in June and a secondary maximum during

September–October, characteristic of the West African monsoon. Since the June 2026 event occurred during the first rainfall peak, our attribution analysis is restricted to this period..

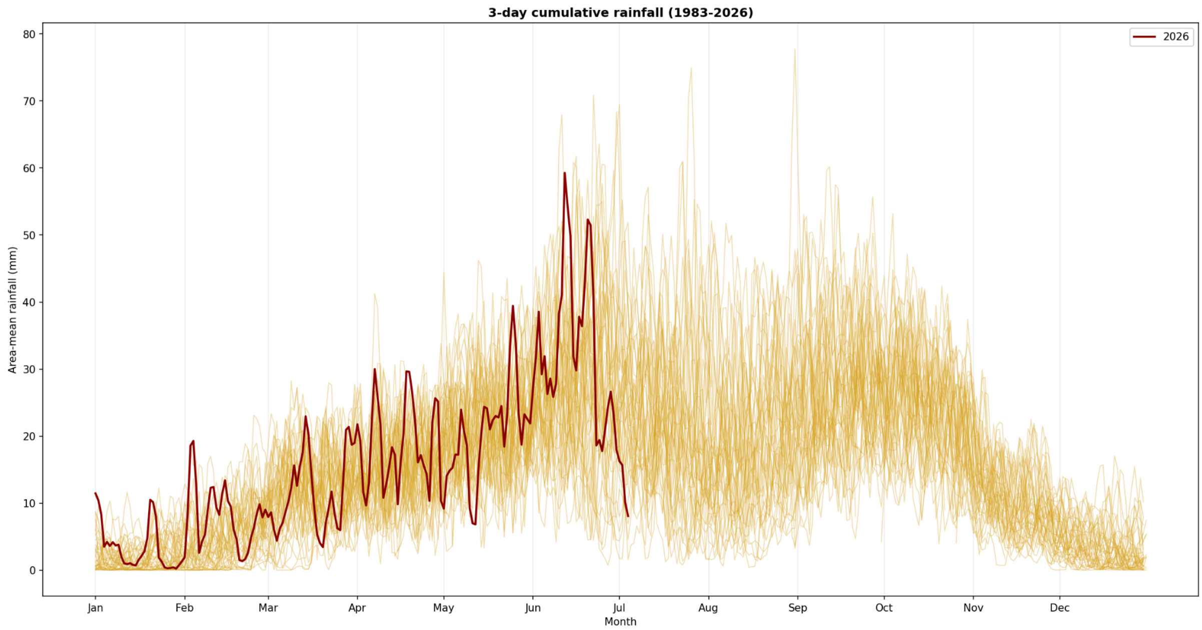

Figure 3. Top: Annual rainfall cycle in the study region. Bottom: Cumulative 3-day precipitation amount with the dark brown color indicating the 2026 annual rainfall cycle.

In this report, we study the influence of anthropogenic climate change by comparing the likelihood and intensity of similar extreme events at present with those in a 1.4°C cooler climate without human-caused warming (based on Forster et al., 2026). We also extend this analysis into the future by assessing the influence of a further 1.4°C of global warming from present. This is in line with the latest Emissions Gap Report from the United Nations Environment Programme, which shows that the world is on track for at least a 2.8°C temperature rise given currently implemented policies (UNEP, 2025).

2 Observed trends

2.1 Trends in gridded data

Four gridded datasets, TAMSAT, MSWEP, ERA5, and CHIRPS, are used in this analysis (see Table 2.1). Three of the datasets (TAMSAT, MSWEP and ERA5) fully cover the event period. For CHIRPS, we use the preliminary version — a near-real-time product, which is available only up to 30 June 2026. This provisional product relies primarily on stations transmitted through the Global Telecommunication System and therefore incorporates substantially fewer gauge observations than the final CHIRPS product. Consequently, considering the few gauge data the June 2026 event is not fully represented in this dataset (Appendix A1) and the resulting trend estimates should be interpreted with caution. The estimated changes in rainfall intensity are more consistent across the observational datasets. ERA5 and MSWEP indicate that the event was approximately 36% more intense in today's climate than it would have been in a 1.4°C cooler climate, while TAMSAT estimates an increase of

26%. As CHIRPS does not include the event, we only use it up to 2025 and thus can only estimate the change in intensity and likelihood for a 3-year event and not estimate the return period for the 2026 event. The three datasets estimate return periods ranging from approximately 2 to 4 years (see table 2.1). Given the overall agreement among the three datasets that fully represent the event, we adopt a 3-year return period for the remainder of the attribution analysis. We note that the choice of return period affects the estimated probability ratios but that the estimated changes in intensity are independent of this.

Table 2.1: Estimated return periods of Rx3day over the southern coast of West Africa for reanalysis datasets (ERA5, MSWEP, TAMSAT) with coverage of the event.

Dataset	Event		GMST	
	Magnitude (mm/day)	Return period (95% C.I.)	Probability Ratio	Change in magnitude (%)
ERA5	**17**	1.9 (1.4, 3.5)	**6.9 (1.37, 3901720)**	**27.79 (5,15, 56.78)**
MSWEP	**18**	4.1 (2.4, 10)	**12.9 (2.05, 5060)**	**35.82 (10.89, 67.98)**
CHIRPS	n/a	n/a	1.2 (0.33, 8.47)	3.81 (-30.36. 28.34)
TAMSAT	**20**	2.5 (1.5, 4.9)	**7.57 (1.03, 10200)**	**26.17 (0.54, 66.53)**

To test for the potential influence of anthropogenic forcing on June-July rainfall, we fit a nonstationary generalised extreme value distribution that scales with global mean surface temperature and evaluate the relative likelihood and intensity of the 2026 event in the present climate, and the climate scaled to 1.4°C cooler (see section A1.3 for full methods). The observational datasets show broadly consistent evidence that heavy three-day rainfall events have become more intense as the climate has warmed (Figures 4 a-d) and give an increase in likelihood between 20% and a factor of 13 and an increase in intensity between 4 and 36% (see table 2.1). Although the confidence intervals are necessarily wide because of the variability of extreme rainfall in the region, all four datasets indicate an increase in the likelihood of such events attributable to anthropogenic warming.

Rx3d: TAMSAT

(a)

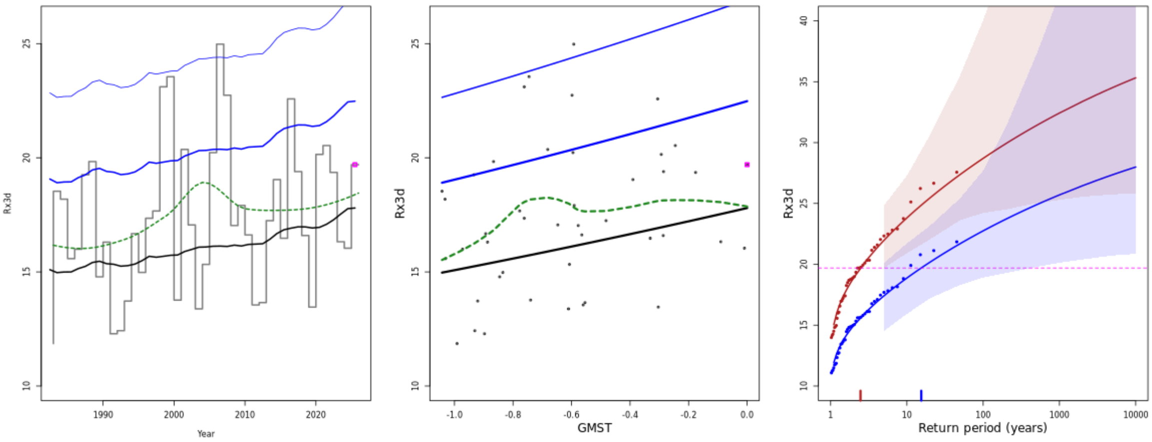

(b)

Rx3d: ERA5

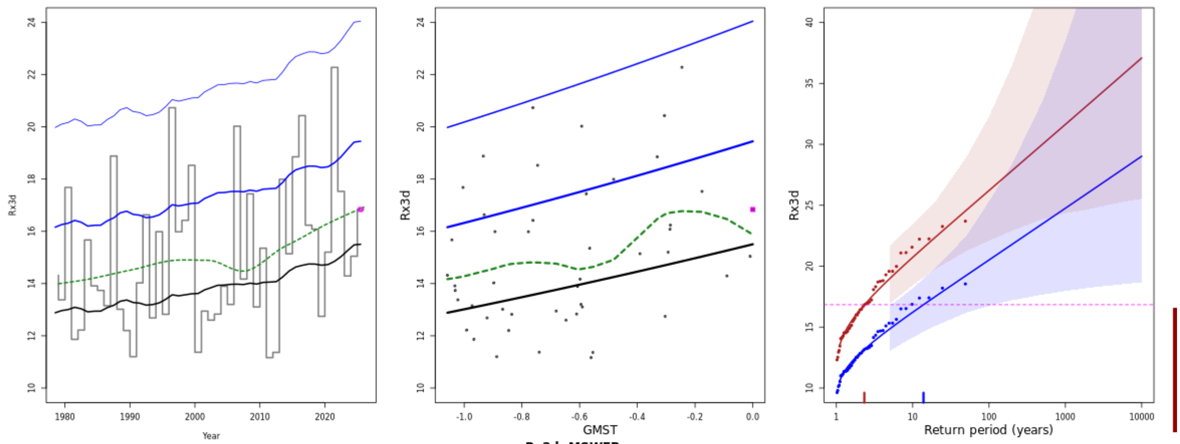

(c)

Rx3d: MSWEP

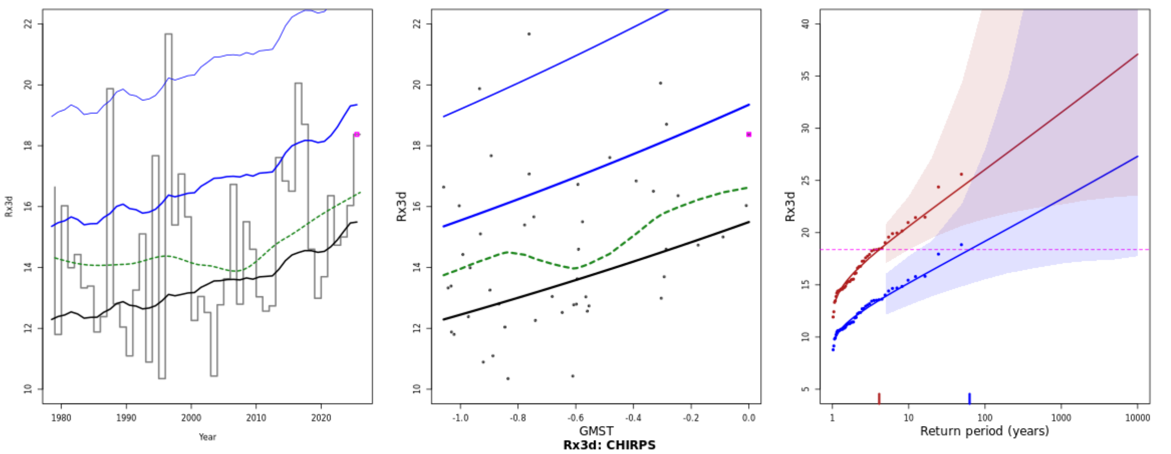

Rx3d: CHIRPS

(d)

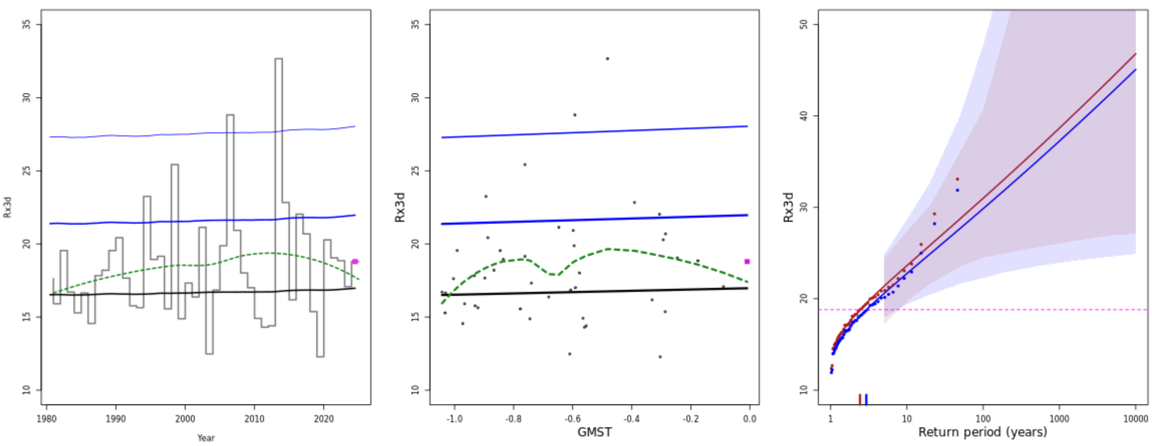

Figure 4. *GEV fit with fixed dispersion parameter scaling proportional to GMST, of June-July Rx3day. The left hand figures show the evolution of annual (Jul-Jun) Rx3day over the West Africa coast overlaid with model estimates. The middle panels show Rx3day as a function of the smoothed GMST. The thick black line denotes the time-varying location parameter. The vertical black lines show the 95% confidence interval for the location parameter, for the current, 2026 climate and the fictional, 1.4ºC cooler climate. The 2026 observation is highlighted with the magenta box. The right hand side panels show the return time plots for the climate of 2026 (red) and a climate with GMST 1.4ºC cooler (blue). The past observations are shown twice: once shifted up to the current climate and once shifted down to the climate of the pre-industrial era. The markers show the data and the lines show the fits and uncertainty from the bootstrap. The magenta line shows the magnitude of the 2026 event analysed here. These are shown for TAMSAT **(a)**, ERA5**(b)**, MSWEP**(c)**,and CHIRPS**(d).***

3 Attribution of trends

3.1 Evaluation of climate models

In the subsections below, we show the results of the model evaluation for each location. The climate models are evaluated against the observations to ascertain their ability to capture:

1. Seasonal cycles: For this, we qualitatively compare the seasonal cycles of precipitation based on model outputs against observation-based cycles. We discard any models that exhibit ill-defined peaks in their seasonal cycles. We also discard the model if the rainy season onset/termination varies significantly from the observations.

2. Spatial patterns: Models that do not match the observations in terms of the large-scale precipitation patterns during June-July are excluded.

3. Parameters of the fitted statistical models. We discard the model if the model and observation parameter ranges do not overlap.

In this study, we evaluated CMIP6, CORDEX and HighResMIP models (see appendix A1.2 for descriptions) on the three criteria listed above. The models are labelled as 'good ', ' reasonable ', or 'bad' based on their performance in terms of the three criteria discussed above. A model is given an overall rating of 'good' if it is rated 'good' for all three characteristics. If there is at least one 'reasonable', then its overall rating will be 'reasonable ', and 'bad' if there is at least one 'bad'. We use all models with label 'good' as well as the models with one or two labels 'reasonable'.' In the study, HighResMIP models performed relatively well compared to CORDEX and CMIP6. For HighResMIP, 6 out of 13 models evaluated passed the test. For CORDEX 12 were retained out of 27 and 10 out of 30 for CMIP6, respectively. Tables of the model evaluation results can be found in Appendix A2.

3.2 Synthesis of results

For the event definitions described above, we evaluate the influence of anthropogenic climate change on the events by calculating the probability ratio as well as the change in intensity using observations and climate models. Models which do not pass the evaluation described above are excluded from the analysis. The aim is to synthesise results from models that pass the evaluation along with the observations-based products, to give an overarching attribution statement. Tables of the results of this model fitting can be found in Appendix A3.

Figures 3.2 a show the changes in probability and intensity for the observations (blue) and models (red). Before combining them into a synthesised assessment, first, a representation error is added (in quadrature) to the observations, to account for the difference between observations-based datasets that cannot be explained by natural variability. This is shown in these figures as white boxes around the light blue bars. The dark blue bar shows the average over the observation-based products. Next, a term to account for intermodel spread is added (in quadrature) to the natural variability of the models. This is shown in the figures as white boxes around the light red bars. The dark red bar shows the model average, consisting of a weighted mean using the (uncorrelated) uncertainties due to natural variability plus the term representing intermodel spread (i.e., the inverse square of the white bars). Observation-based products and models are combined into a single result in two ways. Firstly, we neglect common model uncertainties beyond the intermodel spread that is depicted by the model average, and compute the weighted average of models (dark red bar) and observations (dark blue bar): this is indicated by the magenta bar. As due to common model uncertainties, model uncertainty can be larger than the intermodel spread, secondly, we also show the more conservative estimate of an unweighted, direct average of observations (dark blue bar) and models (dark red bar) contributing 50% each, indicated by the white box around the magenta bar in the synthesis figures.

The synthesis of the observational datasets indicates that an event similar to that observed in 2026 is estimated to be 5.37 times more likely in the current climate than in a climate 1.4°C cooler (95% CI: 0.4–8470), with an estimated increase in rainfall intensity of 22.8% (95% CI: –12.9 to 69.4%). However, the confidence intervals are wide, reflecting the relatively short observational records, large natural variability in West African rainfall, and differences among the observational products. The uncertainty in the observational results is partly driven by differences in the underlying datasets. While ERA5, MSWEP and TAMSAT show broadly consistent year-to-year variability and indicate increasing rainfall intensity, the preliminary CHIRPS dataset does not fully capture the 2026 event because it relies on a limited number of near-real-time gauge observations. Therefore, we only use CHIRPS up to 2025 in the estimation of trends. Despite these differences, the observational datasets consistently suggest an increase in the intensity of extreme rainfall associated with a warmer climate, consistent with Clausius Clapeyron (C-C) scaling.

The climate model results also indicate an increase in the likelihood and intensity of June–July Rx3day rainfall, although the estimated changes are very small compared to those obtained from observations and on average do not capture the C-C scaling which would be expected at about 10% at current warming levels. The finding suggests that events comparable to that of 2026 are 1.18 times more likely (95% CI: 0.62 - 2.58) and approximately 3.5% more intense (95% CI: -8.03 to +16.4%) in the current climate relative to a climate 1.4°C cooler. Individual models show reasonable agreement in the direction of change, although there remains substantial spread in the magnitude of the response, reflecting differences in their representation of convective rainfall and the West African monsoon system.

Figure 3.1: *Synthesised changes in (left) likelihood and (right) changes in intensity of June-July Rx3day in the study region when comparing the 2026 climate and a 1.4°C cooler climate representing the preindustrial past. Observation-based datasets are shown in blue, climate models are shown in red, and the synthesis is shown in magenta.*

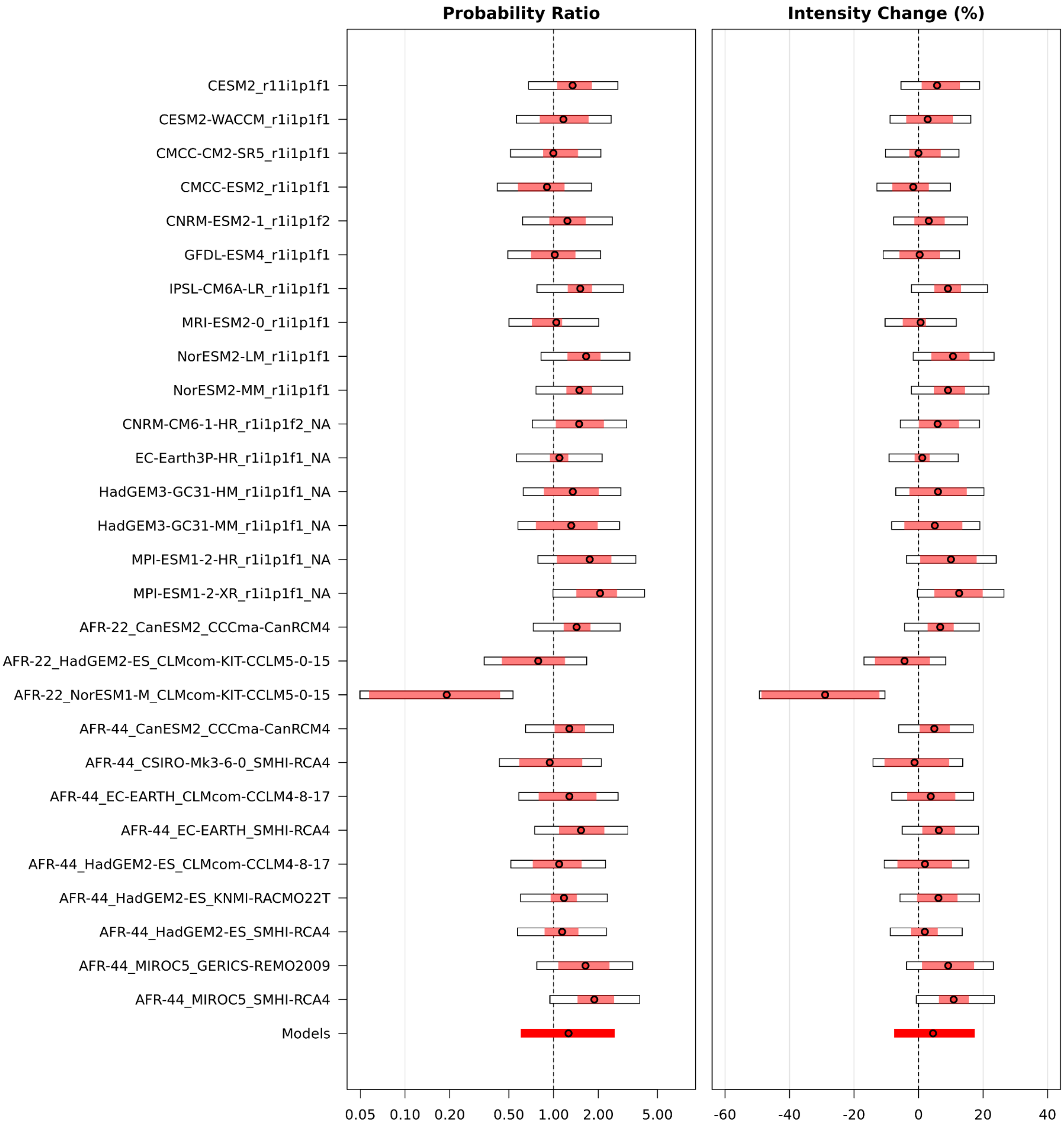

Figure 3.2 Change in probability (left) and intensity (right) for June-July Rx3day in the study region between the current climate and a future, 1.4°C warmer climate..

Table 1.1: *Summary of results for June-July Rx3day, presented in Figs 3.1&3.2: changes due to GMST include past-present changes and present-future changes*

Data	Attributable influence of increases in GMST		
		Probability ratio (95% CI)	**Intensity change (%) (95% CI)**
Observations	**Past- Present**	5.37 (0.394, 8470)	22.8 (-12.9, 69.4)
Models		1.18 (0.622, 2.58)	3.51 (-8.03, 16.4)
Synthesis		1.21 (0.584, 4.43)	5.50 (-10.1, 23.1)
Unweighted Synthesis		2.51 (0.375, 472)	13.2 (-12.8, 43.6)
Models only	**Present- Future**	1.26 (0.643, 2.42)	4.48 (-6.21, 16.1)

Usually, we combine the observational and model evidence to a weighted synthesis. However, given the large uncertainties and systematic underestimation of the observed trends in the models, the quantitative synthesis is probably not very meaningful, as it is weighted strongly towards the climate models. Combining models and observations given both equal weight yields a best estimate that the likelihood of a June–July Rx3day event similar to that observed in 2026 has increased by a factor of 2.5 (95% CI: 0.38–472), while its intensity has increased by approximately 13.2% (95% CI: –12.8 to 43.6%) due to anthropogenic climate change. Although the best estimates indicate a positive influence of climate change on both the probability and intensity of the event, the confidence intervals are very large and encompass no change. This reflects the uncertainty associated with attributing rainfall extremes in West Africa, where observational limitations, and model uncertainties remain important.

To assess how the risk may evolve under continued warming, we also evaluate the event in a future climate representative of a world that is 2.8°C warmer than pre-industrial levels. Owing to the limitations of the available climate models over this relatively small study region, we do not consider it possible to provide a robust quantitative estimate of future changes in the likelihood or intensity of events such as the June 2026 rainfall. Nevertheless, we note that the projected future changes with respect to the present day are consistent with the small (underestimated) increase that was modelled from past to present. Furthermore, the available evidence indicates that the physical conditions conducive to extreme rainfall will continue to strengthen as the climate warms due to the well-established thermodynamic response of the atmosphere, whereby higher temperatures allow the atmosphere to hold more moisture, increasing the potential for intense rainfall (Clausius–Clapeyron scaling). Given that the current risk of flood-inducing rainfall is already substantial, continued warming is expected to maintain, and likely exacerbate, the high flood risk facing the rapidly urbanising coastal regions of West Africa, even if the magnitude of that increase cannot be robustly quantified.

3.3 Conclusions hazard

Overall, the observational and modelling results agree on the direction of change, with both indicating an increase in the likelihood and intensity of extreme 3-day rainfall under a warmer climate. However, the observations suggest a much stronger response than the climate models. This difference is not unexpected and may reflect gridded observational uncertainties as well as model limitations in representing organised convection and the dynamics of the West African monsoon. Taken together, the historical results, future projections, and physical understanding point towards an increase in the likelihood and intensity of extreme 3-day rainfall over the Gulf of Guinea as the climate warms, although the exact magnitude of this increase remains highly uncertain.

4 Vulnerability and exposure

In western Africa, April-May marks the onset of the rainy season in coastal countries which often leads to heavy flooding (Anticipation Hub, 2025). During June 2026, the region experienced episodes of torrential rainfall. At the Accra International Airport meteorological station (Ghana), the observed daily rainfall total ranked as the fourth highest in the 1981–2026 record, while the cumulative rainfall for the month represented the highest June total recorded over the same period (OCHA, 2026, Ghana Business News, 2026). The unanticipated intensity of rainfall caused significant infrastructure damage and fatalities in Côte d'Ivoire; Ghana; Benin; Togo; and Nigeria (OCHA, 2026, Chanatry, 2026). Over 70 people died across 5 countries due to flooding, of which at least 59 lives were lost in Abidjan since mid-May (Wilson, 2026; Karikari, 2026 & OCHA, 2026). In some areas, excessive rainfall along with poor waste management and blocked drainage amplified urban runoff, submerging buildings and displacing thousands of people (Agbo, 2026; Egbejule, 2026, Karikari, 2026). Flooding also triggered electrical infrastructure failures leading to fires in some areas, while in Nigeria, rainwater inundated the international airport, suspending operations (Oyedokun & Onyema, 2026, Egbejule, 2026). As a result, economic activity, agricultural activities and livelihoods were significantly interrupted, causing widespread income losses (RFI, 2026). Furthermore, a potential decline in cocoa yields due to the flooded roads and an increased risk of disease with excessive moisture have resulted in increased prices, impacting global supply (Prior, 2026). West Africa Acute Food Insecurity area-level classifications from May 2026 shows parts of Niger, Nigeria and Cameroon under “stressed” and/ or “crisis” conditions (Integrated Food Security Phase Classification scale) (FEWS NET, 2026). FEWS analysis for food insecurity (August 2024 - January 2025) indicates that shortfalls in agricultural production due to agroclimatic shocks, and trade limitations, makes seasonal flooding a persistent concern that exacerbates food insecurity (FEWS NET, 2024).

Significantly, the spatial and temporal scope is similar to previous fluvial floods in 2024, 2022, and 2012 (Zachariah, 2022). However, each event pushes communities into a more severe socio-economic crisis compounded by extreme weather and other conflicts. The increasing frequency of flooding in the region makes it difficult to fully recover, which exacerbates the effects of subsequent events on communities that are still recovering (Africa Center for Strategic Studies, 2024; Dike et al., 2025, Chanatry, 2026). This section presents a rapid assessment of vulnerability and exposure, with particular attention to the areas experiencing the most severe impacts. It is intended to provide a broad, though non-exhaustive, overview of the drivers of flood risk.

4.1 Sociodemographics

The Human Development Index (HDI) is a metric that indicates relative development, and includes data on life expectancy, education and per capita income. The HDI values are available for the year 2023 for the affected countries Ghana (0.628), Côte d'Ivoire (0.582), Togo (0.571) and Nigeria (0.560) that are categorized as ‘medium human development’ and Benin (0.515) and Liberia (0.510) are classified as ‘low human development’ highlighting the relative vulnerability of countries in the region (UNDP, 2025). In general older adults and young children are most vulnerable and not able to evacuate rapidly (Rufat et al., 2015), and while the former age group in the region is relatively small, the latter represents a larger fraction in the demography of the region (for Ghana and Nigeria the population 0-14 was 35% and 41% respectively, in 2025, substantially higher than the global average of 24%, World Bank, 2026a). Another group vulnerable to flooding impacts are people with disabilities, as they may have limited mobility to evacuate before the flooding or after the flooding has occurred, while sometimes also facing discrimination and systems that are not set up to support them (e.g warnings not accessible for deaf or blind individuals) (Chukwudum et al, 2025; Munyenyembe & Asogwa, 2025). People with pre-consisting health issues are more vulnerable to direct and indirect health impacts of flooding (Alderman et al., 2012). Following a previous flooding event in 2024, that also affected countries in Western Africa, the World Health Organization indicated that there was already a high degree of malnutrition and disrupted health services, mostly affecting women and children who may therefore be even more susceptible to impacts from the floods (WHO Africa, 2024).

4.2 Land-use and land cover change

Over the last three decades in West Africa, there has been a conversion of natural vegetation to croplands, resulting in a decrease in vegetation cover in areas vulnerable to soil degradation (Assede et al., 2023). Population growth in west Africa has been identified as a key driver of land cover change Herrmann et al., 2020). Increases in population growth can drive other changes like increased demand for firewood, charcoal and construction materials, and the need to cultivate additional land to feed larger populations which prompts further increases in land use and landcover changes (Assede et al., 2023). Southwestern Côte d'Ivoire has seen a large shift towards croplands including an expansion of cocoa plantations, illegal logging, and dense road network that is driven by factors like rural to urban migration and population growth, agricultural expansion, wildfires and mining (Kouassi et al., 2021**).** This is illustrative of patterns across the affected area. In Benin a study modelling landcover change found that conversion of natural vegetation to cropland increases flood risk (Hounkpe et al., 2019). Future sustainable development requires land use policies that both address the needs of people and maintain the biodiversity and productivity of natural systems (Assede et al., 2023).

4.3 Urbanization and informality

Across West Africa, urban areas have rapidly expanded, with the percentage of urban population in Ghana increasing from 23% in 1960 to 59% in 2025, with an even larger percent increase from 14% urban population in 1960 to 64% in 2025 for Nigeria (World Bank, 2026b). In particular, coastal areas have been the focus of economic development due to rich natural resources and business opportunities. The rapid population growth puts a strain on existing infrastructure, results in unplanned development, and increases the exposure and vulnerability of millions of people to flood risk.

Many of West Africa's fastest growing urban areas are built around low-lying coastal lagoons such as Abidjan in Côte d'Ivoire and Lagos in Nigeria (Davies-Vollum et al, 2025). With growing populations and unplanned development, the physical infrastructure encroaches on lagoon habitats, reducing their natural capacity to accommodate water (Davies-Vollum et al, 2025). This, along with urban drainage and waste management issues, and sea level rise, increase flood risk (Davies-Vollum et al, 2025).

Large populations live in informal settlements around urban areas, including 4.8 million people in Ghana and 52.6 million people in Nigeria, as estimated by UN-Habitat (2020), for the year 2018. Urban flood risk in West African cities is intensified by unregulated expansion into wetlands, flood retention areas, and riparian zones, as well as by fragmented infrastructure provision and governance (Andreasen et al., 2022). A systematic review of flood risk management in West Africa finds that settlement expansion into flood-prone areas and river modification are recurring drivers, while spatial planning, local knowledge, and early warning systems are repeatedly recommended but still limited in use (Wagner et al., 2021).

In Nigeria’s capital Lagos, people living in informal settlements are highly vulnerable to flooding (Adelekan, 2010). Besides the direct effect of floods on people living in informal settlements, there are also significant subsequent impacts because many people in informal settlements are not able to sustain their income (*“Flooding makes people go hungry for days”* as quoted by Douglas et al., 2008, for men living in informal settlements of Accra, Ghana).

In the areas of Agbogbloshie, Old Fadama and Glefe in Ghana, vulnerability to floods is intensified by inadequate drainage, development on wetlands, poor housing materials, limited sanitation, insecure tenure and weak access to public infrastructure (Amoako, et al., 2017). Informal areas repeatedly experience floods, with governance issues contributing to increasing risk as existing policies are unevenly enforced and safe and affordable housing alternatives are limited (Mensah et al., 2025; Amoako, et al., 2017). In Old Fadama, residents face recurring floods, limited long-term relief from coping strategies, and eviction threats undermine adaptive capacity (Abunyewah et al., 2022). In addition, unclear and conflicting land-tenure arrangements contribute to flood vulnerability because they allow settlements to grow without planning, weaken residents’ claims to infrastructure and services, while raising the risk of eviction (Amoako, et al., 2017). Along with physical drainage and infrastructure, access to safe and affordable housing, improved infrastructure and services in informal areas, and planning that includes informal communities is needed to reduce vulnerability (Amoako, et al., 2017).

4.4 Flood risk management

4.4.1 Governance, policies, plans and infrastructure

Flood risk management in West Africa is primarily led by national agencies. In Ghana, flood risk management is coordinated through a multi-agency framework. The Ghana Meteorological Agency (GMet) provides meteorological monitoring and weather warnings, the Ghana Hydrological Authority undertakes hydrological monitoring and flood forecasting, while NADMO leads disaster preparedness, emergency response, relief and recovery. In Côte d'Ivoire, ONPC, GSPM and ONAD play similar roles while SODEXAM provides weather and climate information. Similarly, NiMet and Nigeria Hydrological Services provide weather and flood forecasting in Nigeria, while the national weather and climate information agencies in Togo and Bénin are Meteo Togo and Meteo Benin respectively. Both Ghana and Côte d'Ivoire have strengthened flood management after recent severe urban floods. Ghana developed a flood contingency plan for Greater Accra in 2024 (UNDP, 2024), and Côte d'Ivoire validated a national flood risk profile in 2025 to support urban and land-use planning (UNDRR, 2025). Nevertheless, flood management remains largely reactive, with limited preventive action.

Flood protection measures like Ghana’s Akosombo Dam on the Volta River that reduced flooding for decades, encouraged people to settle on floodplains until the emergency water release in 2023 that displaced over 30,000 people (UNDRR, 2023). The Keta Sea Wall in Ghana protected the Keta town but increased coastal erosion in nearby communities by disrupting natural sand movement (World Bank, 2017). Similarly, the Vridi Canal in Abidjan, Côte d'Ivoire altered coastal processes and contributed to erosion elsewhere (World Bank, 2020). Abidjan's drainage programme (ONAD) is limited by insufficient funding, showing a potential soft limit to adaptation because economic and institutional constraints prevent adequate protection. The development of flood management infrastructure is the dominant form of adaptation in the region, including drainage construction, raised buildings, river dredging and channelisation in some regions (Wagner et al, 2021). While important, physical infrastructure is not enough to eliminate flood risk and therefore a range of residual risks remain (Wagner et al, 2021).

4.4.2 Early warning and early action

The Climate Outlook for the April-May-June season indicated near-average to below average conditions in much of Ghana, Côte d'Ivoire, Togo, Benin and Nigeria (AGRHYMET CCR-AOS, 2026). Only the southwestern most part of Côte d'Ivoire was expected to receive above average rainfall. Nigeria Hydrological Services Agency (NIHSA) Annual Flood Outlook released in April warned more than 14,000 communities across 33 states in Nigeria where flooding was predicted to peak between July and September (NIHSA, 2026). Furthermore, the National Economic Council (NEC) authorised the release of nearly 60 million USD (~N83.2 billion) for the Anticipatory Action Task Force on 18 June so as to prepare for flooding, and early action intervention against extreme weather events (Office of The Vice President, 2026). At the time of writing, it is unclear whether there were special warnings issued by SODEXAM (Côte d'Ivoire) or GMet (Ghana) closer to the event. However, regular updates and warnings were issued at the onset of the event. In Ghana, a warning was issued on the morning of 29 June to alert of flood risks following the intense rains (Ministry of the Interior, 2026), a "Severe Severity" alert was issued on July 1 in Liberia and in Côte d'Ivoire SODEXAM published a yellow alert for 22 - 24 June (SODEXAM, 2026, Liberia Met Service, 2026). While Early Warning Systems exist in some countries (e.g. FEWS Ghana), their effectiveness is limited by forecasting constraints, unreliable data and inaccessibility to rural regions (Katsekpor et al., 2025). Additionally, early warning dissemination remains inconsistent, with reports and warnings observed more in Nigeria (Sumaina, 2026). NEMA supported early warning campaigns, stakeholder engagement (with local committees) and national flood response indicating a shift towards anticipatory action and proactive preparedness (Abdulrazaq, 2026; Philip, 2026). Recently, a flash flood risk map and advisory indicating runoff risks in Nigeria from 1 to 10 July and a Continental Multi-Hazard & Advisory Bulletin for 10-14 July have been published by NiMet and ACDMA respectively (Ni Met, 2026; ACDMA, 2026). Additionally, a Situation report flood risks in West and Central Africa (July 2023) too indicates general flood risk assessment of certain areas (UNOCHA, 2023).

4.4.3 Emergency response

Following the flooding, the President of Ghana released nearly 17 million USD (~200 million cedis)for flood relief, humanitarian aid and ordered the removal of buildings constructed near waterways. The 10th and 11th of July were identified as national cleanup days (Wilson, 2026). After identifying relocation sites as an emergency response to the ongoing flooding and city evictions in Côte d'Ivoire, the government announced on July 1 that 12,000 housing units will be built on Northern Highway and in Songon to relocate 60,000 affected people (RFI, 2026; Official Portal of the Government of Côte d'Ivoire, 2026). In Accra, more than 400 people were rescued by the Greater Accra Regional Fire Command and other evacuation operations were carried out by NADMO, Ghana Armed Forces, military personnel, and local volunteers (Wilson, 2026). In Nigeria, FFS, Federal Road Safety Corps, National Emergency Management Agency (NEMA) and Nigeria Security and Civil Defence Corps (NSCDC) conducted national rescue operations (Abdulrazaq, 2026). Through field teams, the Red Cross, and other partner organizations, the National Disaster Management Agency (NDMA) has activated its flood preparedness and response system in Liberia (Deemie, 2026).

4.4.4 Individual and household coping behaviors

Evidence on coping capacity to floods across West Africa remains limited, with available studies concentrated in Nigeria, constraining broader regional understanding. This highlights the need for more geographically diverse research, including how strategies vary across different socioeconomic and governance contexts. Nevertheless, the available studies provide important insights into the mechanisms households employ to respond to flood impacts. Informal social networks consistently emerge as a critical source of immediate assistance, with support from relatives, neighbours, and friends often preceding formal government intervention (Nabegu, 2014). Individuals and households also adopt a range of coping strategies, including selling assets, borrowing money, seeking paid employment, and temporary rural-urban migration (Nabegu, 2014). In Accra, Ghana coping measures included digging trenches around homes, constructing temporary barriers, and using rocks, sandbags and concrete to divert flood waters (Owusu et al, 2023).

Coping capacity is further shaped by socioeconomic disparities, with differences in access to financial resources, flood-resistant infrastructure, and emergency relief influencing households' ability to absorb and recover from flood impacts (Mobalaji et al., 2025). Households with more financial resources and access to assistance can generally absorb losses more easily, while households with fewer resources may need to sell assets, borrow money, migrate or reduce food consumption (Erman et al., 2020; Akukwe et al., 2023). While households also implement structural and behavioral adaptation measures through self-help and community initiatives, these are often limited in effectiveness, underscoring the need for more transformative approaches to strengthening flood resilience (Adegun, 2023).

4.4.5 Insurance and social protection

West African countries have increasingly adopted shock-responsive social protection to address climate-related hazards by scaling up social safety nets and combining long-term poverty reduction with rapid emergency support. For instance, Ghana leveraged its LEAP and Ghana School Feeding programmes during COVID-19 and the 2015 floods (Ministry of Gender, Child and Social Protection, 2023). Nigeria used the NASSP and NCTP and piloted anticipatory cash transfers for flood-affected households in 2022 (Red Cross Red Crescent Climate Centre, 2022). Côte d'Ivoire deployed its Productive Social Safety Net Programme in response to floods in the Cavally region in 2024 (World Bank, 2025). Although parametric flood insurance schemes exist in Nigerian states like Lagos (UNDP, 2026), evidence of scaling-up social protection programmes in response to the ongoing floods across the region remains limited, highlighting the need for more adaptive and shock-responsive social protection systems to address vulnerabilities exacerbated by climate hazards.

4.5 V&E conclusions

This region of West Africa is particularly vulnerable to flood risks due to a variety of risk drivers. The coastal belt is highly populated with rapid population growth and urbanisation over several decades and with cities located in low-lying lagoons prone to flooding. Urbanization puts increasing pressure on urban infrastructure, leads to unplanned growth of informal areas and increases the number of people at risk during a flood event. The flooding has a cascading impact in the region, affecting both formal and informal economic activity, disrupting supply chains, and increasing the likelihood of waterborne illness and food insecurity. These types of floods and associated impacts will continue to occur unless significant efforts are made to reduce vulnerability and exposure to the floods. Solutions are not easy; they require improvements across a range of areas such as increasing access to safe and affordable housing, improving drainage and sanitation systems, enforcing policies on safer construction, improving early warning dissemination, and greater participation of affected communities in planning.

5 Conclusions

Together, this assessment shows that the interaction of climate change with vulnerability and exposure factors is increasing flood risk in western Africa. Without substantial mitigation and adaptation action, that risk will continue to grow as climate change leads to more extreme rainfall and urbanization continues to increase the exposure of people in flood-prone areas. These findings reinforce the need for mitigation and adaptation to avoid further losses and damages from floods. It also raises questions about the potential for soft limits to adaptation to emerge where financial, institutional and governance constraints limit the adoption and effective implementaiton of adaptation options at scale.

Data availability

All time series used in the attribution analysis are available via the Climate Explorer.

Acknowledgements

This work used JASMIN, the UK's collaborative data analysis environment (https://www.jasmin.ac.uk).

This work used Imperial College Research Computing Service, DOI: 10.14469/hpc/2232.

This work used the KNMI Climate explorer web tool (https://climexp.knmi.nl/start.cgi).

This work used station data for Abidjan

References

All references are given as hyperlinks in the text.

Appendices

A1 Data and methods

A1.1 Observational data

We first use observational and reanalysis data to estimate the return period of a similar event in the present day and to assess the historical trends with increasing GMST. The datasets used are as follows:

ERA5 - The European Centre for Medium-Range Weather Forecasts' 5th generation reanalysis product, ERA5, is a gridded dataset that combines historical observations into global estimates using advanced modelling and data assimilation systems (Hersbach et al., 2020). We use daily rainfall data from this product at a resolution of 0.25°×0.25°, from the years 1950 to present.

We used Extended ERA5 for July 2026; the reanalysis is available until the end of June 2026. We extend the reanalysis data with the ECMWF analysis (month year) and the ECMWF forecast (1 - 6 July) to cover the period of the event

MSWEP - The Multi-Source Weighted-Ensemble Precipitation v2.8 dataset (updated from Beck et al., 2019) is fully global, available at 3-hourly intervals and at 0.1° spatial resolution, available from 1979 to ~3 hours from real-time. This product combines gauge-, satellite-, and reanalysis-based data, including ERA5

CHIRPS - The rainfall product developed by the UC Santa Barbara Climate Hazards Group called "Climate Hazards Group InfraRed Precipitation with Station data" (CHIRPS; Funk et al. 2015). Daily data are available at 0.05° resolution, from 1981-31 May 2026. The product incorporates satellite imagery with in-situ station data. We used the preliminary version —a near-real-time product, which is available only up to 30 June 2026 to check the event.

TAMSAT - The Tropical Applications of Meteorology using SATellite and ground based observations, Maidment et al., (2017), is a daily rainfall dataset based on using high-resolution thermal-infrared observations to identify precipitating clouds. Daily rainfall data are available at 0.0375° x 0.0375° spatial resolution over the African continent from 1983 to the present.

Covariate

For this analysis, we use only one covariate. As a measure of anthropogenic climate change we use the (low-pass filtered) global mean surface temperature (GMST), where GMST is taken from the National Aeronautics and Space Administration (NASA) Goddard Institute for Space Science (GISS) surface temperature analysis (GISTEMP, Hansen et al., 2010 and Lenssen et al. 2019). To remove the effect of the El Niño - Southern Oscillation on global mean temperatures, we use a four-year running mean of the GMST, centred on the third year.

A1.2 Model and experiment descriptions

We use three ensembles of climate models from climate modelling experiments using very different framings (Philip et al., 2020): Sea Surface Temperature (SST) driven global circulation high resolution models, coupled global circulation models and regional climate models.

CORDEX

Coordinated Regional Climate Downscaling Experiment CORDEX-CORE over the Africa domain with 0.22 km resolution (AFR-22;Giorgi and Gutowski, 2015; Giorgi et al., 2021) and with 0.44 km resolution (AFR-44; Nikulin et al., 2012). The ensemble used consists of AFR-22 and AFR-44 together with different combinations of 7 regional climate models and downscaling 11 GCMS, resulting in 37 combinations. These simulations are composed of historical simulations up to 2005, and extended to the year 2100 using the RCP8.5 scenario.

2. CMIP6. This consists of simulations from 24 participating models with varying resolutions. For more details on CMIP6, see Eyring et al., (2016). For all simulations, the period 1850 to 2014 is based on historical simulations, while the SSP5-8.5 scenario is used for the remainder of the 21st century.

3. HighResMIP SST-forced model ensemble (Haarsma et al. 2016), the simulations for which span from 1950 to 2050. The SST and sea ice forcings for the period 1950-2014 are obtained from the 0.25° x 0.25° Hadley Centre Global Sea Ice and Sea Surface Temperature dataset that have undergone area-weighted regridding to match the climate model resolution. For the 'future' time period (2015-2050), SST/sea-ice data are derived from RCP8.5 (CMIP5) data, and combined with greenhouse gas forcings from SSP5-8.5 (CMIP6) simulations (see Section 3.3 of Haarsma et al. 2016 for further details).

A1.3 Statistical methods

Methods for observational and model analysis and for model evaluation and synthesis are used according to the World Weather Attribution Protocol, described in Philip et al., (2020), with supporting details found in van Oldenborgh et al., (2021), Ciavarella et al., (2021), Otto et al., (2024) and here. The key steps, presented in sections 3-6, are: (3) trend estimation from observations; (4) model validation; (5) multi-model attribution; and (6) synthesis of the attribution statement.

In this report we analyse the time series of June-July seasonal maxima of 3-day accumulated rainfall (June-July Rx3day), area-averaged over the study region described in Section 1.2. A nonstationary Generalised Extreme Value (GEV) distribution is used to model June-July Rx3day. For rainfall, the distribution is assumed to scale exponentially with the covariates, with the dispersion (the ratio between the standard deviation and the mean) remaining constant over time, to account for the dependence of maximum moisture content that the atmosphere can hold in accordance with the Clausius-Clayperon relationship (Trenberth et.al., 2003, O'Gorman and Schneider 2009). The parameters of the statistical model are estimated using maximum likelihood.

For each time series we calculate the return period and intensity of the event under study for the 2026 GMST and for 1.4°C cooler GMST: this allows us to compare the climate of now and of the preindustrial past without human-caused warming (based on Forster et al., 2026), by calculating the probability ratio (PR; the factor-change in the event's probability) and change in intensity of the event.

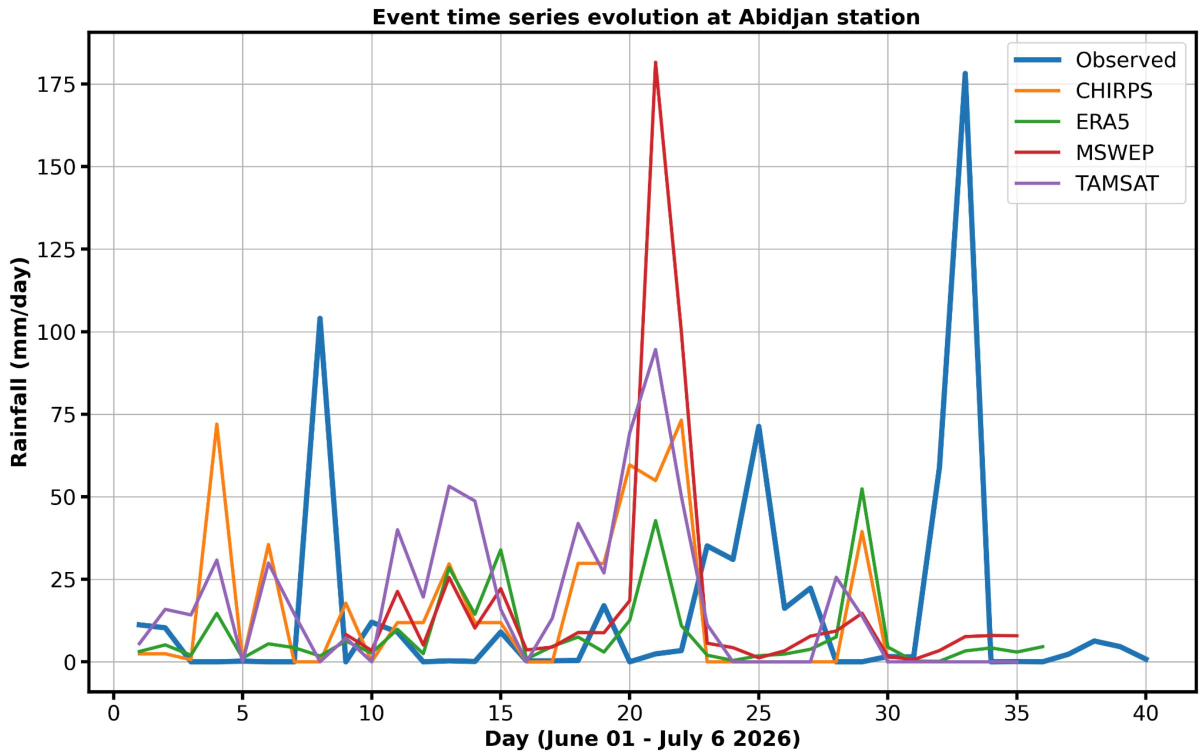

A1. Showing temporal evolution of June-July flood event over Adidjan station in Cote in in situ data versus gridded datasets at nearest grid point

A2 Model evaluation

Figure A.2. to A.2. show the seasonal cycle and spatial patterns for all models. Table A3.1 shows evaluation values. On the Table we only show models that passed the evaluation test

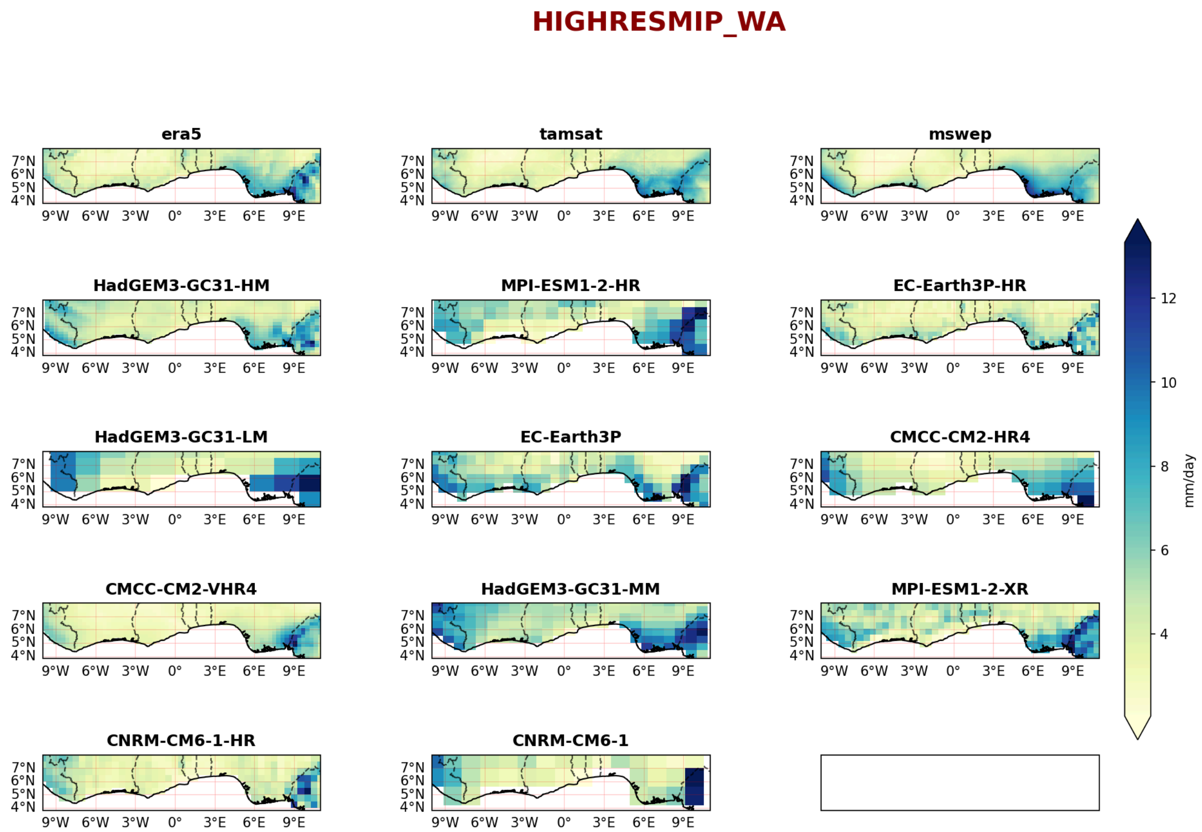

Figure A.2.1: *Spatial patterns of June-July precipitation in observations and HIGHRESMIP models.*

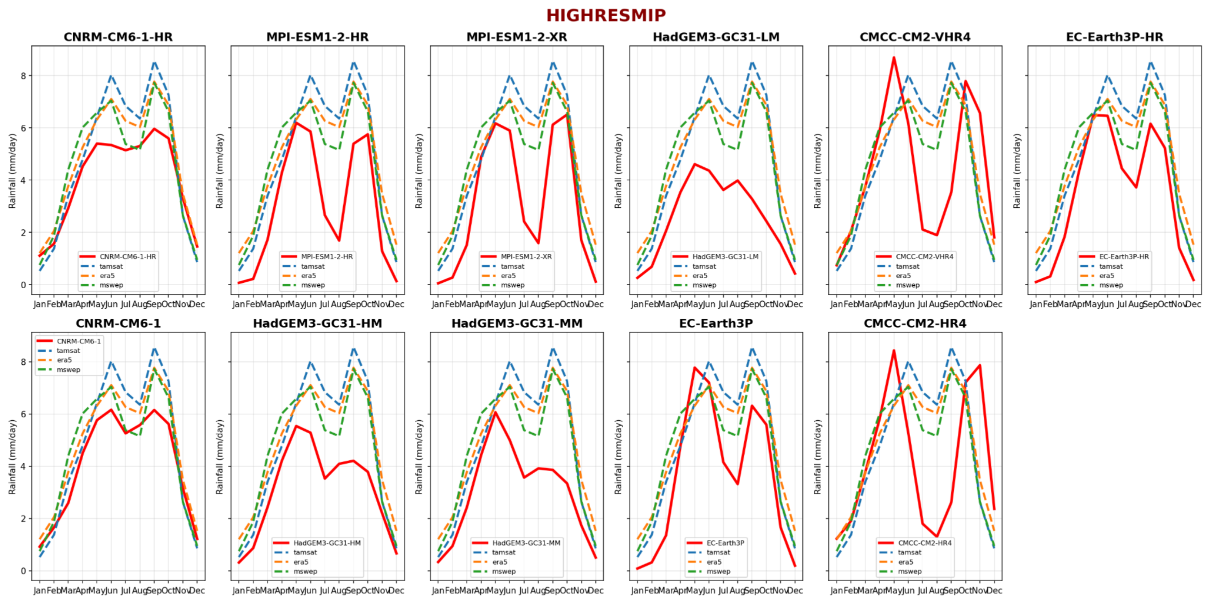

Figure A.2.2: *Seasonal cycles of precipitation in observations shown in dotted lines, and HIGHRESMIP models, shown in red.*

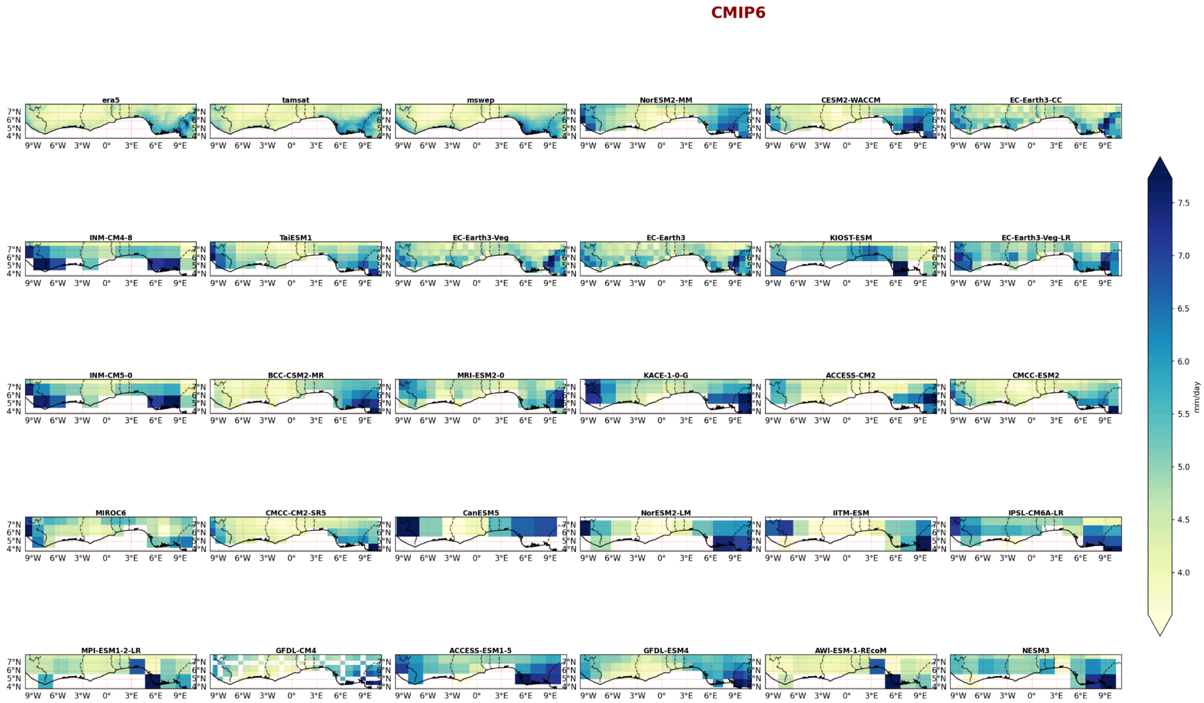

Figure A.2.3: Spatial patterns of June-July precipitation in observations and CMIP6 models.

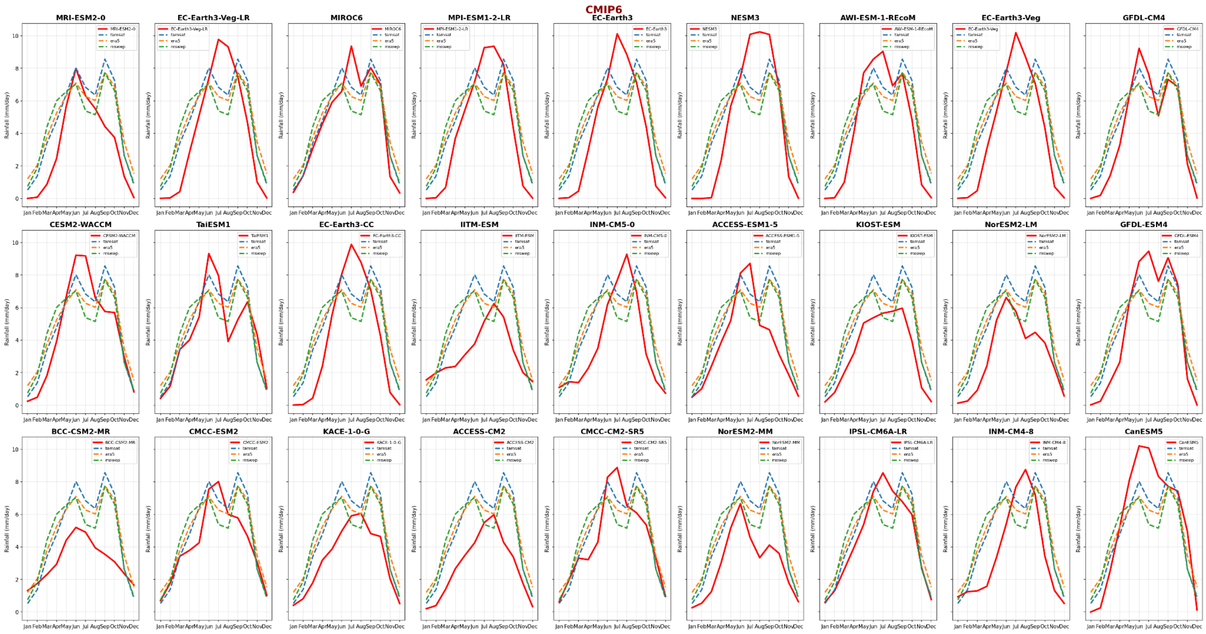

Figure A.2.4: Seasonal cycles of precipitation in observations shown in dotted lines, and CMIP6 models, shown in red.

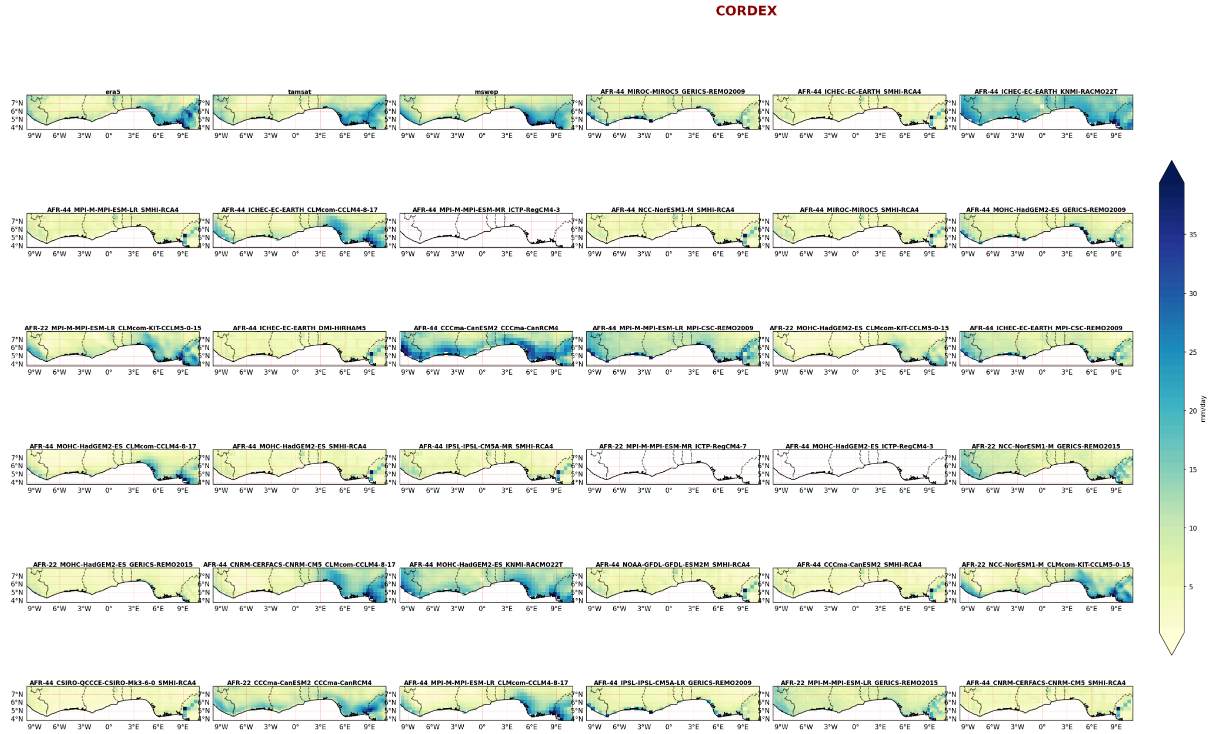

Figure A.2.5: Spatial patterns of June-July precipitation in observations and CORDEX models.

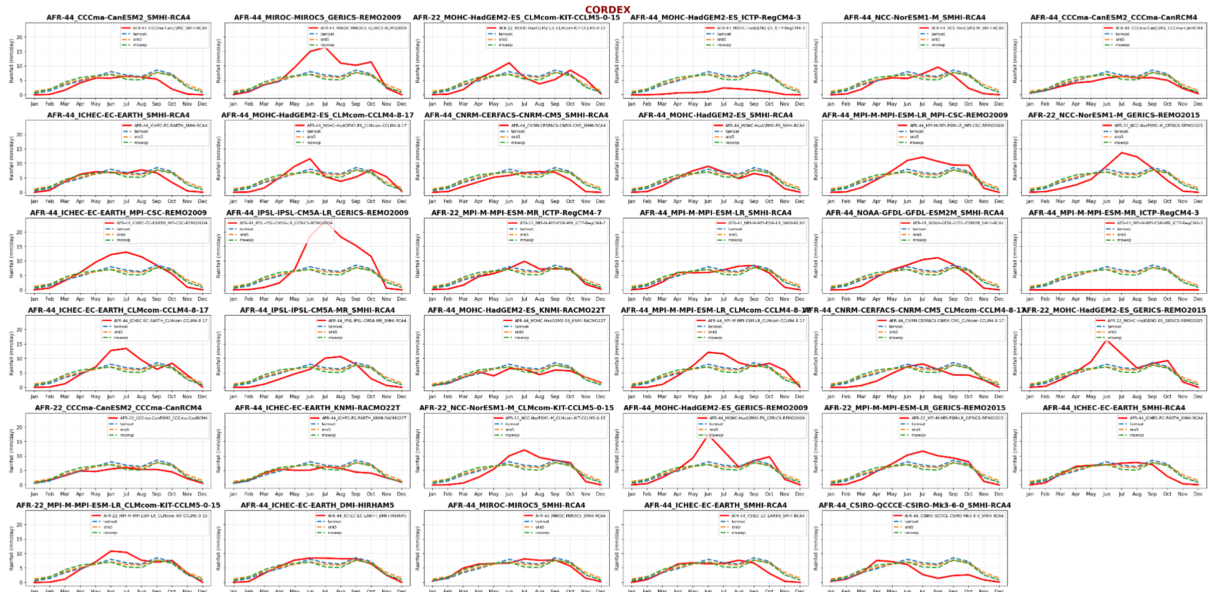

Figure A.2.6: Seasonal cycles of precipitation in observations shown in dotted lines, and CORDEX models, shown in red.

Table A3.1: Evaluation results of the climate models considered for attribution analysis of June-July Rx3day. For each model, the threshold for a 1-in-3-year event is shown, along with the best estimates of the Dispersion and Shape parameters are shown, along with 95% confidence intervals. Furthermore evaluation of the seasonal cycle and spatial pattern are shown.

Model / Observations	Seasonal cycle	Spatial pattern	Dispersion	Shape parameter	Conclusion
era5			0.149 (0.114 ...	0.0031 (-0.27	

			0.185)	... 0.25)	
mswep			0.145 (0.0962 ... 0.176)	0.0093 (-0.27 ... 0.43)	
tamsat			0.169 (0.128 ... 0.194)	-0.11 (-0.36 ... 0.26)	
chirps			0.169 (0.113 ... 0.201)	0.026 (-0.26 ... 0.38)	
CNRM-CM6-1-HR_r1i1p1f2_NA ()	good	good	0.123 (0.0954 ... 0.147)	-0.17 (-0.56 ... 0.028)	good
EC-Earth3P-HR_r1i1p1f1_NA ()	reasonable	reasonable	0.119 (0.112 ... 0.125)	-0.056 (-0.12 ... 0.0084)	reasonable (2)
HadGEM3-GC31-HM_r1i1p1f1_NA ()	reasonable	reasonable	0.161 (0.101 ... 0.201)	0.12 (-0.057 ... 0.54)	reasonable (2)
HadGEM3-GC31-MM_r1i1p1f1_NA ()	reasonable	reasonable	0.174 (0.136 ... 0.204)	-0.069 (-0.42 ... 0.20)	reasonable (2)
MPI-ESM1-2-HR_r1i1p1f1_NA ()	reasonable	reasonable	0.169 (0.108 ... 0.219)	-0.21 (-0.70 ... 0.064)	reasonable (2)
MPI-ESM1-2-XR_r1i1p1f1_NA ()	reasonable	reasonable	0.132 (0.0960 ... 0.163)	-0.23 (-0.61 ... 0.099)	reasonable (2)
AFR-22_CanESM2_CCCma-CanRCM4 ()	good	reasonable	0.100 (0.0531 ... 0.133)	0.51 (0.12 ... 1.3)	reasonable (2)
AFR-22_HadGEM2-ES_CLMcom-KIT-CCLM5-0-15 ()	good	reasonable	0.205 (0.155 ... 0.245)	-0.10 (-0.50 ... 0.19)	reasonable
AFR-22_NorESM1-M_CLMcom-KIT-CCLM5-0-15 ()	reasonable	reasonable	0.160 (0.107 ... 0.206)	0.34 (-0.17 ... 0.88)	reasonable (2)
AFR-44_CanESM2_CCCma-CanRCM4 ()	good	reasonable	0.157 (0.104 ... 0.193)	0.21 (-0.023 ... 0.62)	reasonable (1)
AFR-44_CSIRO-Mk3-6-0_SMHI-RCA4 ()	reasonable	reasonable	0.158 (0.0854 ... 0.201)	0.20 (-0.040 ... 0.92)	reasonable (2)
AFR-44_EC-EARTH_CLMcom-CCLM4-8-17 ()	reasonable	reasonable	0.109 (0.0674 ... 0.140)	0.067 (-0.42 ... 0.65)	reasonable (2)
AFR-44_EC-EARTH_SMHI-RCA4 ()	reasonable	reasonable	0.0988 (0.0560 ... 0.124)	0.37 (0.029 ... 1.2)	reasonable (2)

AFR-44_HadGEM2-ES_CLMcom-CCLM4-8-17 ()	reasonable	good	0.248 (0.160 ... 0.296)	-0.13 (-0.42 ... 0.36)	reasonable (2)
AFR-44_HadGEM2-ES_KNMI-RACMO22T ()	good	good	0.212 (0.113 ... 0.271)	0.59 (0.12 ... 1.9)	reasonable (1)
AFR-44_HadGEM2-ES_SMHI-RCA4 ()	reasonable	reasonable	0.109 (0.0676 ... 0.137)	0.31 (-0.082 ... 0.81)	reasonable (2)
AFR-44_MIROC5_GERICS-REMO2009 ()	reasonable	good	0.160 (0.113 ... 0.192)	0.029 (-0.42 ... 0.39)	reasonable (1)
AFR-44_MIROC5_SMHI-RCA4 ()	good	good	0.108 (0.0514 ... 0.141)	0.52 (0.17 ... 1.8)	reasonable (1)
CESM2_r11i1p1f1 ()	reasonable	reasonable	0.181 (0.146 ... 0.202)	0.050 (-0.081 ... 0.15)	reasonable (2)
CESM2-WACCM_r1i1p1f1 ()	reasonable	good	0.177 (0.159 ... 0.202)	-0.24 (-0.36 ... -0.15)	reasonable (1)
CMCC-CM2-SR5_r1i1p1f1 ()	reasonable	good	0.173 (0.149 ... 0.185)	-0.16 (-0.23 ... -0.028)	reasonable (1)
CMCC-ESM2_r1i1p1f1 ()	reasonablereasonable	good	0.168 (0.153 ... 0.199)	-0.11 (-0.20 ... -0.029)	reasonable (1)
CNRM-ESM2-1_r1i1p1f2 ()	reasonable	good	0.148 (0.122 ... 0.159)	-0.17 (-0.32 ... 0.00043)	reasonable (1)
GFDL-ESM4_r1i1p1f1 ()	good	good	0.194 (0.181 ... 0.213)	-0.14 (-0.31 ... -0.0035)	good
IPSL-CM6A-LR_r1i1p1f1 ()	reasonable	good	0.187 (0.171 ... 0.210)	0.068 (-0.11 ... 0.14)	reasonable (1)
MRI-ESM2-0_r1i1p1f1 ()	reasonable	reasonable	0.144 (0.121 ... 0.164)	-0.034 (-0.055 ... 0.12)	reasonable (2)
NorESM2-LM_r1i1p1f1 ()	good	reasonable	0.181 (0.151 ... 0.207)	0.074 (-0.049 ... 0.16)	reasonable (1)
NorESM2-MM_r1i1p1f1 ()	good	reasonable	0.201 (0.173 ... 0.215)	-0.081 (-0.25 ... -0.012)	reasonable (2)

A3 Estimated trends in climate models

This section shows Probability Ratios and change in intensity ΔI for models that passed model evaluation and also includes the values calculated from the fits with observations.

Table A3.2. Event magnitude, probability ratio and change in intensity for 3-year return period for Rx3day for observational datasets and each model that passed the evaluation tests. (a) from pre-industrial climate to the present and (b) from the present to 2.8℃ above pre-industrial climate.

(a)

Model / Observations	**Threshold for return period 3-yr**	**Probability ratio PR [-]**	**Change in intensity ΔI [%]**

era5	17 mm/day	6.9 (1.4 ... 3.9e+6)	28 (5.2 ... 57)
mswep	18 mm/day	13 (2.0 ... 5.1e+3)	36 (11 ... 68)
tamsat	20 mm/day	7.6 (1.0 ... 1.0e+4)	26 (0.55 ... 67)
chirps	14 mm/day	1.2 (0.33 ... 8.5)	3.8 (-30 ... 28)
CNRM-CM6-1-HR_r1i1p1f2_NA ()	11 mm/day	2.7 (0.95 ... 12)	13 (-0.70 ... 25)
EC-Earth3P-HR_r1i1p1f1_NA ()	10 mm/day	1.1 (0.99 ... 1.2)	0.97 (-0.086 ... 1.9)
HadGEM3-GC31-HM_r1i1p1f1_NA ()	10 mm/day	0.80 (0.42 ... 2.0)	-4.6 (-20 ... 14)
HadGEM3-GC31-MM_r1i1p1f1_NA ()	11 mm/day	1.8 (0.60 ... 6.9)	9.4 (-8.8 ... 27)
MPI-ESM1-2-HR_r1i1p1f1_NA ()	9.7 mm/day	1.5 (0.54 ... 83)	5.1 (-10 ... 28)
MPI-ESM1-2-XR_r1i1p1f1_NA ()	8.4 mm/day	1.0 (0.52 ... 5.4)	0.10 (-9.9 ... 13)
AFR-22_CanESM2_CCCma-CanRCM4 ()	12 mm/day	1.7 (1.3 ... 2.3)	9.9 (4.3 ... 15)
AFR-22_HadGEM2-ES_CLMcom-KIT-CCLM5-0-15 ()	18 mm/day	0.71 (0.43 ... 1.5)	-7.5 (-21 ... 6.8)
AFR-22_NorESM1-M_CLMcom-KIT-CCLM5-0-15 ()	16 mm/day	0.47 (0.34 ... 1.3)	-17 (-30 ... 4.3)
AFR-44_CanESM2_CCCma-CanRCM4 ()	11 mm/day	1.1 (0.83 ... 1.9)	2.6 (-3.6 ... 12)
AFR-44_CSIRO-Mk3-6-0_SMHI-RCA4 ()	12 mm/day	1.6 (0.65 ... 4.7)	9.9 (-9.2 ... 33)
AFR-44_EC-EARTH_CLMcom-CCLM4-8-17 ()	25 mm/day	1.4 (0.64 ... 4.7)	4.5 (-6.9 ... 16)
AFR-44_EC-EARTH_SMHI-RCA4 ()	11 mm/day	1.0 (0.67 ... 1.9)	0.15 (-5.7 ... 9.4)
AFR-44_HadGEM2-ES_CLMcom-CCLM4-8-17 ()	23 mm/day	1.6 (0.71 ... 4.4)	9.6 (-8.6 ... 27)
AFR-44_HadGEM2-ES_KNMI-RACMO22T ()	14 mm/day	1.1 (0.84 ... 1.5)	5.3 (-5.9 ... 16)
AFR-44_HadGEM2-ES_SMHI-RCA4 ()	13 mm/day	0.94 (0.57 ... 1.5)	-0.90 (-7.5 ... 5.3)
AFR-44_MIROC5_GERICS-REMO2009 ()	28 mm/day	2.0 (0.94 ... 8.5)	11 (-0.98 ... 28)
AFR-44_MIROC5_SMHI-RCA4 ()	13 mm/day	1.8 (1.4 ... 2.7)	12 (6.0 ... 19)

#REF!	#REF! mm/day	1.3 (0.87 ... 2.4)	4.5 (-2.5 ... 14)
CMIP6 ()	#REF! mm/day	1.1 (0.92 ... 1.5)	2.1 (-1.4 ... 5.9)
ACCESS-CM2_r1i1p1f1 ()	14 mm/day	0.84 (0.66 ... 1.2)	-3.0 (-7.6 ... 2.2)
AWI-ESM-1-REcoM_r1i1p1f1 ()	13 mm/day	0.82 (0.60 ... 1.1)	-3.4 (-9.2 ... 2.1)
BCC-CSM2-MR_r1i1p1f1 ()	34 mm/day	1.4 (0.97 ... 3.6)	4.8 (-0.47 ... 14)
CMCC-CM2-SR5_r1i1p1f1 ()	17 mm/day	1.4 (0.90 ... 1.7)	5.0 (-2.0 ... 8.8)
EC-Earth3-Veg-LR_r1i1p1f1 ()	14 mm/day	1.7 (1.3 ... 2.9)	9.7 (4.0 ... 16)
INM-CM4-8_r1i1p1f1 ()	17 mm/day	0.64 (0.48 ... 0.96)	-7.2 (-13 ... -0.91)
IPSL-CM6A-LR_r1i1p1f1 ()	20 mm/day	2.2 (1.3 ... 3.7)	13 (4.2 ... 21)
KACE-1-0-G_r1i1p1f1 ()	13 mm/day	1.7 (0.83 ... 2.3)	11 (-4.3 ... 17)

(b)

Model	**Threshold for return period 10 yr**	**Probability ratio PR [-]**	**Change in intensity ΔI [%]**
CNRM-CM6-1-HR_r1i1p1f2_NA ()	11.4484145762486 mm/day	1.5 (1.1 ... 2.0)	5.9 (1.4 ... 11)
EC-Earth3P-HR_r1i1p1f1_NA ()	10.1542007175573 mm/day	1.1 (1.0 ... 1.2)	1.1 (0.099 ... 2.1)
HadGEM3-GC31-HM_r1i1p1f1_NA ()	10.2178248047273 mm/day	1.3 (0.92 ... 1.9)	6.0 (-1.5 ... 14)
HadGEM3-GC31-MM_r1i1p1f1_NA ()	11.1326511034345 mm/day	1.3 (0.81 ... 1.9)	5.0 (-3.1 ... 12)
MPI-ESM1-2-HR_r1i1p1f1_NA ()	9.68892804901929 mm/day	1.8 (1.1 ... 2.3)	10 (1.8 ... 17)
MPI-ESM1-2-XR_r1i1p1f1_NA ()	8.35521155265053 mm/day	2.1 (1.5 ... 2.5)	13 (6.2 ... 19)
AFR-22_CanESM2_CCCma-CanRCM4 ()	11.5409705891607 mm/day	1.4 (1.3 ... 1.7)	6.7 (4.1 ... 9.5)
AFR-22_HadGEM2-ES_CLMcom-KIT-CCLM5-0-15 ()	17.7321638116629 mm/day	0.79 (0.48 ... 1.1)	-4.3 (-12 ... 2.1)
AFR-22_NorESM1-M_CLMcom-KIT-CCLM5-0-15 ()	16.2235252447809 mm/day	0.19 (0.061 ... 0.41)	-29 (-47 ... -13)
AFR-44_CanESM2_CCCma-CanRCM4 ()	10.9478916162939 mm/day	1.3 (1.1 ... 1.5)	4.9 (1.7 ... 8.3)
AFR-44_CSIRO-Mk3-6-0_SMHI-RCA	11.5743814176011 mm/day	0.94 (0.63 ... 1.5)	-1.3 (-9.2 ... 8.2)

4 ()			
AFR-44_EC-EARTH_CLMcom-CCLM4-8-17 ()	24.8838920148589 mm/day	1.3 (0.85 ... 1.8)	3.8 (-2.2 ... 10)
AFR-44_EC-EARTH_SMHI-RCA4 ()	10.9228296380481 mm/day	1.5 (1.2 ... 2.1)	6.3 (2.5 ... 9.9)
AFR-44_HadGEM2-ES_CLMcom-CCLM4-8-17 ()	22.7638929733858 mm/day	1.1 (0.77 ... 1.4)	2.0 (-5.2 ... 9.0)
AFR-44_HadGEM2-ES_KNMI-RACMO22T ()	14.4566805641305 mm/day	1.2 (1.0 ... 1.3)	6.2 (0.88 ... 11)
AFR-44_HadGEM2-ES_SMHI-RCA4 ()	13.3031350367764 mm/day	1.1 (0.93 ... 1.4)	1.9 (-0.95 ... 4.6)
AFR-44_MIROC5_GERICS-REMO2009 ()	27.8594939914796 mm/day	1.6 (1.1 ... 2.2)	9.2 (2.4 ... 16)
AFR-44_MIROC5_SMHI-RCA4 ()	13.1413882284062 mm/day	1.9 (1.5 ... 2.4)	11 (7.6 ... 14)
CMIP6 ()			
ACCESS-CM2_r1i1p1f1 ()	13.5444841068964 mm/day	1.0 (0.91 ... 1.4)	-1.7 (-6.8 ... 1.9)
AWI-ESM-1-REcoM_r1i1p1f1 ()	12.6720680084947 mm/day	0.90 (0.62 ... 1.1)	3.2 (0.0092 ... 6.8)
BCC-CSM2-MR_r1i1p1f1 ()	33.7210114655045 mm/day	1.2 (1.0 ... 1.5)	7.8 (5.8 ... 9.3)
CMCC-CM2-SR5_r1i1p1f1 ()	16.9823677715595 mm/day	1.0 (0.75 ... 1.3)	8.0 (4.7 ... 10)
EC-Earth3-Veg-LR_r1i1p1f1 ()	14.4544808849971 mm/day	1.5 (1.3 ... 1.7)	3.1 (2.0 ... 5.9)
INM-CM4-8_r1i1p1f1 ()	17.1910503888779 mm/day	1.0 (0.76 ... 1.1)	12 (9.5 ... 13)
IPSL-CM6A-LR_r1i1p1f1 ()	20.3530782076701 mm/day	1.7 (1.3 ... 1.9)	9.1 (6.1 ... 13)
KACE-1-0-G_r1i1p1f1 ()	13.1648577136865 mm/day	1.5 (1.3 ... 1.7)	5.0 (1.1 ... 6.9)